
Quantification of model error for inverse problems in the Weak Neural Variational Inference framework

Vincent C. Scholz^a, P.S. Koutsourelakis^{a,b}

^a Technical University of Munich, Professorship of Data-driven Materials Modeling, School of Engineering and Design, Boltzmannstr. 15, Garching, Germany

^b Munich Data Science Institute (MDSI - Core member), Garching, Germany
vincent.scholz@tum.de, p.s.koutsourelakis@tum.de

Abstract

We present a novel extension of the Weak Neural Variational Inference (WNVI) framework for probabilistic material property estimation that explicitly quantifies model errors in PDE-based inverse problems. Traditional approaches assume the correctness of all governing equations, including potentially unreliable constitutive laws, which can lead to biased estimates and misinterpretations. Our proposed framework addresses this limitation by distinguishing between reliable governing equations, such as conservation laws, and uncertain constitutive relationships. By treating all state variables as latent random variables, we enforce these equations through separate sets of residuals, leveraging a virtual likelihood approach with weighted residuals. This formulation not only identifies regions where constitutive laws break down but also improves robustness against model uncertainties without relying on a fully trustworthy forward model. We demonstrate the effectiveness of our approach in the context of elastography, showing that it provides a structured, interpretable, and computationally efficient alternative to traditional model error correction techniques. Our findings suggest that the proposed framework enhances the accuracy and reliability of material property estimation by offering a principled way to incorporate uncertainty in constitutive modeling.

1 Introduction

Inverse problems arise in various scientific and engineering disciplines, including medical imaging, which are crucial in reconstructing hidden properties from indirect measurements. One important application is elastography [1, 2], a technique used to infer the mechanical properties of soft tissues, aiding in disease diagnosis and treatment planning. Elastography data acquisition typically involves applying mechanical forces to tissue and measuring the resulting displacements using imaging modalities such as ultrasound, magnetic resonance imaging (MRI) [3], or optical coherence tomography [4].

Solving the inverse problem in elastography requires computational methods to extract meaningful mechanical properties from noisy and often incomplete displacement (or strain) data. Broadly, these methods fall into Bayesian and non-Bayesian approaches. Non-Bayesian approaches focus on finding a single best-fit solution. Physics-Informed Neural Networks (PINNs) [5] integrate physical laws into deep learning models to enforce consistency with governing equations, offering flexibility in handling complex tissue structures, though at the cost of high computational demands and sensitivity to training data quality. Traditional deterministic optimization methods [6], such as finite element-based approaches, directly minimize a cost function representing the difference between observed and predicted data. These well-established methods lack uncertainty quantification and may converge to local minima. In contrast, Bayesian techniques, such as Markov Chain Monte

Carlo (MCMC) [7] and Variational Inference (VI) [8], aim to estimate probability distributions over the solution space, providing uncertainty quantification. MCMC offers rigorous statistical estimates but is computationally expensive, while VI is more efficient but introduces approximation errors.

Multiple sources of error influence the accuracy of inverse elastography reconstructions. Measurement noise arises from the limitations of imaging techniques, leading to uncertainty in displacement data. Bayesian approaches handle these effects systematically and account for the uncertainty they introduce. The more delicate part is model errors [9]. These arise when the mathematical formulation of a model fails to capture the full complexity of the underlying physical process [10], posing a significant challenge in elastography due to the variety of biological tissue types involved [11]. Various strategies have been proposed to address these errors, which can be broadly categorized into external correction methods, internal correction methods, model selection approaches, and machine learning-based approaches.

External correction methods, such as the Kennedy and O’Hagan (KOH) framework [12], introduce an additive discrepancy term—often modeled as a Gaussian process—to adjust model predictions based on observed data. While this approach provides a flexible way to account for discrepancies, it lacks physical interpretability [13] and does not generalize well to other material properties beyond those explicitly corrected [14]. In elastography, where enforcing physical constraints such as equilibrium and conservation laws is essential, external correction methods may lead to inconsistencies in the reconstructed mechanical parameters.

Internal correction methods, in contrast, aim to incorporate uncertainty directly within the model structure by modifying its parameters. Parameter Uncertainty Inflation (PUI) techniques [15, 16], such as Sargsyan’s parameter embedding [17, 18], introduce stochastic variability into model parameters, ensuring that uncertainty is consistently propagated to all inferred quantities. This approach enables more physically consistent uncertainty quantification by embedding model structural errors rather than treating them as additive corrections. Additionally, PUI allows uncertainty to be meaningfully extrapolated to different observables or model scenarios, enhancing predictive reliability. However, these methods introduce computational complexity due to high-dimensional posterior sampling [15].

An alternative strategy is model selection, where competing models are quantitatively compared to determine which best explains the observed data. Bayesian model comparison techniques, such as Bayes factors [19], provide a rigorous statistical framework for ranking models. Still, their application in elastography is limited by the computational cost of evaluating high-dimensional probability distributions. Additionally, selecting the best-fitting model does not necessarily resolve underlying model inaccuracies, which may lead to biased estimates of tissue properties if all considered models are inadequate.

An alternative to model-based inverse methods in elastography is learning the material law directly from measurement data, bypassing errors introduced by predefined constitutive models. The Auto-progressive Method (AutoP) [20, 21] achieves this by integrating finite element analysis with neural networks to extract stress-strain relationships from force-displacement measurements. This approach offers greater flexibility in capturing complex, heterogeneous tissue behavior without imposing restrictive assumptions. However, while AutoP ensures physical consistency through embedded mechanical principles, its high computational cost and numeric instabilities remain a significant challenge [21].

The proposed framework provides a probabilistic approach to material property estimation by distinguishing between reliable governing equations, such as conservation laws, and less reliable constitutive laws [22, 23]. Unlike traditional model-based methods that assume the correctness of all equations, this framework quantifies model errors and identifies regions where the constitutive law may not hold. Incorporating stress as a state variable alongside displacement ensures a more comprehensive representation of tissue mechanics. Furthermore, it leverages a virtual likelihood [24] to incorporate weighted residuals [25]. The method addresses the fundamental limitations of traditional and data-driven approaches, providing a structured, probabilistic alternative for material property estimation in elastography. Compared to existing model error correction techniques, this framework offers several advantages:

- It explicitly identifies regions where constitutive laws break down, enhancing interpretability.
- It does not rely on a fully trustworthy forward model, making it more robust to modeling uncertainties.

- It avoids black-box terms, allowing for more efficient parameter estimation through variational inference.

The remainder of this paper is organized as follows: In section 2, we introduce the forward and Bayesian inverse problem for elastography, followed by a detailed presentation of our methodology, including the derivation of the evidence lower bound (ELBO) and the form of the approximate posterior. Next, in section 3, we validate the efficiency of our approach through numerical experiments. Finally, in section 4, we conclude with a summary and outlook.

2 Methodology

2.1 Problem definition

In this report, we will focus on an inverse problem in model-based elastography, which is governed by a PDE and boundary conditions

$$\nabla \cdot \boldsymbol{\sigma}(\mathbf{s}) = 0, \quad \mathbf{s} \in \Omega \subset \mathbb{R}^d, \quad (1)$$

$$\mathbf{u}(\mathbf{s}) = \mathbf{g}, \quad \mathbf{s} \in \partial\Omega \subset \mathbb{R}^{d-1} \quad (2)$$

$$\boldsymbol{\sigma} \cdot \mathbf{n} = \mathbf{f}, \quad \mathbf{s} \in \partial\Omega \subset \mathbb{R}^{d-1} \quad (3)$$

where $\boldsymbol{\sigma}$ is the Cauchy stress tensor as a function of space \mathbf{s} , \mathbf{n} is the outward normal vector on the boundary, and \mathbf{g} and \mathbf{f} are the respective prescribed values on the boundary. These equations are generally designed to model the physical reality and are general and well-established. We will refer to them as conservation laws and assume that these equations are reliable. We further have a point-wise (local) constitutive law

$$\boldsymbol{\sigma}(\mathbf{s}) = \boldsymbol{\sigma}(\nabla \mathbf{u}(\mathbf{s}); m(\mathbf{s})), \quad (4)$$

where \mathbf{u} is the displacement field and m is the material parameter (field), linking those quantities with the stresses $\boldsymbol{\sigma}$. These governing equations are valid only for specific material classes and rely on assumptions about the material, which may be incorrect. The equations become unreliable if the assumed constitutive model fails to represent the actual material behavior (e.g., assuming linearity for a nonlinear material). In these cases, results might be erroneous or even misleading. We will refer to this as unreliable constitutive law.

With this set of equations, one can typically solve a forward model calculating an output \mathbf{u} from a known input m plus boundary conditions and abstractly denote this as $\mathbf{u}(m)$. In the inverse problem, noisy displacement observations $\hat{\mathbf{u}} = \{\hat{u}_i\}_{i=1}^{N_{\hat{\mathbf{u}}}}$ at locations $\hat{\mathbf{s}} = \{\hat{s}_i\}_{i=1}^{N_{\hat{\mathbf{u}}}}$ are available, where each measurement relates to the solution of the forward problem by

$$\hat{u}_i(\hat{s}_i) = u_i(m, \hat{s}_i) + \tau^{-0.5} \epsilon_i, \quad \epsilon_i \sim \mathcal{N}(\mathbf{0}, \mathbf{1}), \quad (5)$$

where the additive term accounts for the stochastic observation noise, which is assumed to be Gaussian distributed with variance τ^{-1} . We can score how likely the observations $\hat{\mathbf{u}}$ arose from a given material field m in probabilistic terms in the likelihood and can then use Bayes theorem by introducing a prior $p(m)$ to yield the posterior

$$\begin{aligned} p(m|\hat{\mathbf{u}}) &\propto p(\hat{\mathbf{u}}|m) p(m) \\ &\propto \prod_{i=1}^{N_{\hat{\mathbf{u}}}} \mathcal{N}(\hat{u}_i | \mathbf{u}_i(m), \tau^{-1}) p(m). \end{aligned} \quad (6)$$

2.2 Main idea

We propose to reformulate a PDE-based inverse problem where, in addition to inferring the desired input quantity, one should be able to identify the validity of unreliable equations and provide quantitative indicators of model errors over the problem domain. For this, we distinguish between reliable equations (e.g., conservation law, which is typically well-known, physics-based governing equations) and unreliable equations (e.g., constitutive law, which might be selected as part of a design choice). We will propose a scheme based on the ideas presented in [25], which includes reformulating the inverse problem that obviates the need for a forward model while retaining the valuable information the governing PDE provides. However, in addition, we consider *all* state

variables as random variables to be able to enforce reliable and unreliable equations in two separate sets of residuals.

We use a finite-dimensional representation of the material field m , the displacement field \mathbf{u} and the stress field $\boldsymbol{\sigma}$

$$m(\mathbf{x}, \mathbf{s}) = \sum_{i=1}^{d_x} x_i \eta_i^x(\mathbf{s}), \boldsymbol{\sigma}(\chi, \mathbf{s}) = \sum_{i=1}^{d_\chi} \chi_i \boldsymbol{\eta}_i^\chi(\mathbf{s}), \quad \text{and} \quad \mathbf{u} = \sum_{i=1}^{d_u} z_i \boldsymbol{\eta}_i^u(\mathbf{s}) \quad (7)$$

where \mathbf{s} are the spacial coordinates, $\mathbf{z} = \{z_i\}_{i=0}^{d_z}$, $\boldsymbol{\chi} = \{\chi_i\}_{i=0}^{d_\chi}$ and $\mathbf{x} = \{x_i\}_{i=0}^{d_x}$ are the respective (input) parameters, and η_i^x , $\boldsymbol{\eta}_i^u(\mathbf{s})$ and $\boldsymbol{\eta}_i^\chi(\mathbf{s})$ are given basis functions dependent on space.

As in [25], we will make use of the weighted residuals (based on the weak form of the PDE in Eq. 1) to enforce the conservation law

$$r_w^{(e)}(\boldsymbol{\chi}) = \int_{\Omega} \sigma_{ij} w_{i,j} d\Omega - \int_{\Gamma_N} g_i w_i d\Gamma_N, \quad (8)$$

where each residual differs in the selection of its weight function w . As in previous works, the weighted residuals serve as data sources rather than as a means to derive a conventional discretized system of equations. Will further introduce a second set of residuals to score the validity of the constitutive law

$$r^{(c)}(\mathbf{x}, \mathbf{z}, \boldsymbol{\chi}, \mathbf{s}) = \boldsymbol{\sigma}(\boldsymbol{\chi}, \mathbf{s}) - \tilde{\boldsymbol{\sigma}}(\mathbf{x}, \mathbf{z}, \mathbf{s}), \quad (9)$$

where we distinguish between $\boldsymbol{\sigma}$ directly constructed by the random variable $\boldsymbol{\chi}$ (see Eq. 7) and $\tilde{\boldsymbol{\sigma}}$ calculated using the proposed (potentially erroneous) constitutive law in Eq. 4. Further, the conservation law residual is calculated as an integral over a domain, while the constitutive law residual is evaluated at collocation points $\tilde{\mathbf{s}}$.

Alike in [25, 24], we will now treat *both* sets of residuals as *virtual* observations $\hat{r}^{(e)} = \hat{r}^{(e)} = 0$, handling them similarly to the displacement observations in Eq. 5, which relates to the actual residuals as:

$$0 = \hat{r}_j^{(e)} = r_{w^{(j)}}^{(e)}(\boldsymbol{\chi}) + \left(\lambda^{(e)}\right)^{-1} \epsilon_j, \quad \epsilon_j \sim \mathcal{N}(0, 1), \quad \text{and} \quad (10)$$

$$0 = \hat{r}_k^{(c)} = r^{(c)}(\mathbf{z}, \mathbf{x}, \boldsymbol{\chi}, \mathbf{s}) + \left(\lambda_k^{(c)}\right)^{-1} \epsilon_k, \quad \epsilon_k \sim \mathcal{N}(0, 1). \quad (11)$$

If we denote separately all the *virtual* observables $\hat{\mathbf{R}}^{(e)} = \{\hat{r}_k^{(e)} = 0\}_{k=1}^{N_e}$ and $\hat{\mathbf{R}}^{(c)} = \{\hat{r}_j^{(c)} = 0\}_{j=1}^{N_e}$, the equation above gives rise to the *virtual* likelihoods:

$$p(\hat{\mathbf{R}}^{(e)} | \boldsymbol{\chi}) = \prod_{j=1}^{N_e} p(\hat{r}_j^{(e)} = 0 | \boldsymbol{\chi}) \quad (12)$$

$$\propto \prod_{j=1}^{N_e} \sqrt{\lambda^{(e)}} \exp\left(-\frac{\lambda^{(e)}}{2} \left(r_{w^{(j)}}^{(e)}(\boldsymbol{\chi})\right)^2\right), \quad \text{and} \quad (13)$$

$$p(\hat{\mathbf{R}}^{(c)} | \mathbf{z}, \mathbf{x}, \boldsymbol{\chi}, \boldsymbol{\lambda}^{(c)}) = \prod_{h=1}^{N_e} p(\hat{r}_j^{(c)} = 0 | \mathbf{z}, \mathbf{x}, \boldsymbol{\chi}, \boldsymbol{\lambda}^{(c)}) \quad (14)$$

$$\propto \prod_{j=1}^{N_e} \sqrt{\lambda_j^{(c)}} \exp\left(-\frac{\lambda_j^{(c)}}{2} \left(r^{(c)}\right)^2(\mathbf{z}, \mathbf{x}, \boldsymbol{\chi})\right). \quad (15)$$

where both hyper-parameter $\{\lambda^{(e)}, \boldsymbol{\lambda}^{(c)}\} > 0$ penalize the deviation of the residuals from 0, i.e. the value they would attain for any solution tuple $\{\mathbf{z}, \mathbf{x}, \boldsymbol{\chi}\}$ (or equivalently m , $\boldsymbol{\sigma}$ and \mathbf{u}). Note that $\lambda^{(e)}$ describes how tightly we want to enforce the PDE, similar to the numerical tolerance of a deterministic iterative solver. In contrast, $\boldsymbol{\lambda}^{(c)}$ scores the discrepancy (in residual form) between the probabilistic stresses $\boldsymbol{\sigma}$ and the constitutive-law predicted stresses $\tilde{\boldsymbol{\sigma}}$. Thus, the random variables $\boldsymbol{\lambda}^{(c)}$ are central in this framework, as they connect the probabilistic threads between the reliable and unreliable equations of the model. Once the model is converged, a low $\left(\lambda_i^{(c)}\right)^{-1}$ indicates a part of the domain where the selected constitutive law is incorrect and vice versa.

As in [25], the *actual* likelihood is now given by

$$p(\hat{\mathbf{u}}|\mathbf{z}) = \prod_{i=1}^{N_{\hat{\mathbf{u}}}} \mathcal{N}(\hat{u}_i | u_i(\mathbf{z}), \tau^{-1}) \propto \prod_{i=1}^{N_{\hat{\mathbf{u}}}} \sqrt{\tau} e^{-\frac{\tau}{2}(\hat{u}_i - u_i(\mathbf{z}))^2}, \quad (16)$$

which we can implement in the Bayes rule to yield the joint posterior

$$p(\mathbf{x}, \mathbf{z}, \boldsymbol{\chi}, \boldsymbol{\lambda}^{(c)} | \hat{\mathbf{R}}^{(c)}, \hat{\mathbf{R}}^{(e)}, \hat{\mathbf{u}}) = \frac{p(\hat{\mathbf{u}}|\mathbf{z}) p(\hat{\mathbf{R}}^{(e)}|\boldsymbol{\chi}) p(\hat{\mathbf{R}}^{(c)}|\mathbf{z}, \mathbf{x}, \boldsymbol{\chi}, \boldsymbol{\lambda}^{(c)}) p(\mathbf{x}, \mathbf{z}, \boldsymbol{\chi}, \boldsymbol{\lambda}^{(c)})}{p(\hat{\mathbf{R}}^{(c)}, \hat{\mathbf{R}}^{(e)}, \hat{\mathbf{u}})}, \quad (17)$$

with joint prior $p(\mathbf{x}, \mathbf{z}, \boldsymbol{\chi}, \boldsymbol{\lambda}^{(c)})$ and model evidence $p(\hat{\mathbf{R}}^{(c)}, \hat{\mathbf{R}}^{(e)}, \hat{\mathbf{u}})$. In the following, we will adopt a mean field prior for simplicity.

Remarks:

- As the validity of the corresponding constitutive model equations is unknown a priori, the parameters $\boldsymbol{\lambda}^{(c)}$ must be learned from the data.
- If we consider collocation-type residuals, then large values of $(\lambda_j^{(c)})^{-1}$ indicate locations where the model error is high and vice versa. In such a case, nonzero values of $r^{(c)}$ do not arise due to variability in the material parameters \mathbf{x} but rather due to the inadequacy of the constitutive model to provide sufficient closure to the governing equations.
- Selecting values for $(\lambda^{(e)})^{-1}$ similar to the numerical tolerance of a deterministic iterative solver has proven to be a good strategy.
- The integration over the problem domain can either be carried out deterministically or by Monte Carl.

2.3 Probabilistic inference

As the posterior is not available in closed form due to the residual terms, we opt for a numerical method, specifically Variational Inference. Here, the goal is to fit a parameterized family of densities $q_{\boldsymbol{\xi}}(\mathbf{z}, \mathbf{x}, \boldsymbol{\chi}, \boldsymbol{\lambda}^{(c)})$ with tuneable parameters $\boldsymbol{\xi}$ to the exact posterior by minimizing the KL divergence. Therefore, we construct the ELBO as

$$\begin{aligned} \log p(\hat{\mathbf{R}}^{(e)}, \hat{\mathbf{R}}^{(c)}, \hat{\mathbf{u}}) &= \log \int p(\hat{\mathbf{u}}|\mathbf{z}) p(\hat{\mathbf{R}}^{(e)}|\boldsymbol{\chi}) p(\hat{\mathbf{R}}^{(c)}|\mathbf{z}, \mathbf{x}, \boldsymbol{\chi}, \boldsymbol{\lambda}^{(c)}) p(\mathbf{x}, \mathbf{z}, \boldsymbol{\chi}, \boldsymbol{\lambda}^{(c)}) d\mathbf{z} d\mathbf{x} d\boldsymbol{\chi} d\boldsymbol{\lambda}^{(c)} \\ &\geq \left\langle \log \frac{p(\hat{\mathbf{u}}|\mathbf{z}) p(\hat{\mathbf{R}}^{(e)}|\boldsymbol{\chi}) p(\hat{\mathbf{R}}^{(c)}|\mathbf{z}, \mathbf{x}, \boldsymbol{\chi}, \boldsymbol{\lambda}^{(c)}) p(\mathbf{x}, \mathbf{z}, \boldsymbol{\chi}, \boldsymbol{\lambda}^{(c)})}{q_{\boldsymbol{\xi}}(\mathbf{z}, \mathbf{x}, \boldsymbol{\chi}, \boldsymbol{\lambda}^{(c)})} \right\rangle_{q_{\boldsymbol{\xi}}(\mathbf{z}, \mathbf{x}, \boldsymbol{\chi}, \boldsymbol{\lambda}^{(c)})} \\ &= -\frac{\lambda^{(e)}}{2} \sum_{j=1}^{N_e} \left\langle \left(r_{\mathbf{w}^{(j)}}^{(e)} \right)^2 (\boldsymbol{\chi}) \right\rangle_{q_{\boldsymbol{\xi}}(\mathbf{z}, \mathbf{x}, \boldsymbol{\chi}, \boldsymbol{\lambda}^{(c)})} \\ &\quad - \sum_{k=1}^{N_c} \left\langle \frac{\lambda_k^{(c)}}{2} \left(r_k^{(c)} \right)^2 (\mathbf{z}, \mathbf{x}, \boldsymbol{\chi}) \right\rangle_{q_{\boldsymbol{\xi}}(\mathbf{z}, \mathbf{x}, \boldsymbol{\chi}, \boldsymbol{\lambda}^{(c)})} \\ &\quad - \frac{\tau}{2} \sum_{i=1}^{N_{\hat{\mathbf{u}}}} \left\langle (\hat{u}_i - u_i(\mathbf{z}))^2 \right\rangle_{q_{\boldsymbol{\xi}}(\mathbf{z}, \mathbf{x}, \boldsymbol{\chi}, \boldsymbol{\lambda}^{(c)})} \\ &\quad + \left\langle \log \frac{p(\mathbf{z}, \mathbf{x}, \boldsymbol{\chi}, \boldsymbol{\lambda}^{(c)})}{q_{\boldsymbol{\xi}}(\mathbf{z}, \mathbf{x}, \boldsymbol{\chi}, \boldsymbol{\lambda}^{(c)})} \right\rangle_{q_{\boldsymbol{\xi}}(\mathbf{z}, \mathbf{x}, \boldsymbol{\chi}, \boldsymbol{\lambda}^{(c)})} \\ &= \mathcal{L}(\boldsymbol{\xi}), \end{aligned} \quad (18)$$

where $\langle \cdot \rangle_{q_{\boldsymbol{\xi}}}$ denotes the expectation with respect to $q_{\boldsymbol{\xi}}$. The interpretation of the ELBO terms can be done as follows

- The first term of the ELBO promotes the minimization of the conservation law residuals, satisfying the PDE.
- The second term encourages minimizing the constitutive law residuals, linking the stresses $\tilde{\boldsymbol{\sigma}}$ that satisfy the PDE to match the stresses $\boldsymbol{\sigma}$ that satisfy the chosen constitutive equation.

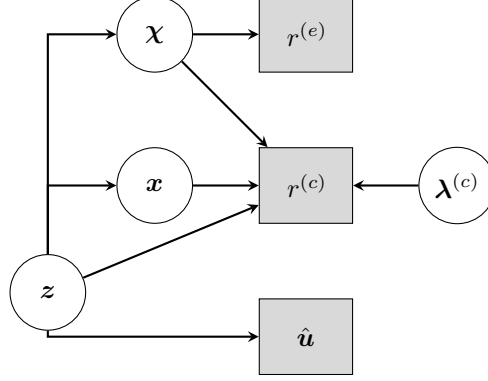


Figure 1: Connection between latents (white circles) and observables (grey boxes).

- The third term minimizes the discrepancy between solution observations \hat{u} and the predicted solution u .
- The fourth term provides regularization by minimizing the KL divergence with the prior.

We follow the works in [25] and perform a Monte Carlo approximation of the first ELBO term by subsampling a set of $K \ll N$ weight functions in each iteration to improve computational efficiency:

$$\sum_{j=1}^{N_e} \left\langle \left(r_{\mathbf{w}^{(j)}}^{(e)} \right)^2 (\boldsymbol{\chi}) \right\rangle_{q_{\xi}(\mathbf{z}, \mathbf{x}, \boldsymbol{\chi}, \boldsymbol{\lambda}^{(c)})} \approx \frac{N_e}{K} \sum_{k=1}^K \left\langle \left(r_{\mathbf{w}^{(j_k)}}^{(e)} \right)^2 (\boldsymbol{\chi}) \right\rangle_{q_{\xi}(\mathbf{z}, \mathbf{x}, \boldsymbol{\chi}, \boldsymbol{\lambda}^{(c)})}, \quad j_k \sim \text{Cat} \left(N_e, \frac{1}{N_e} \right). \quad (19)$$

To ensure a comprehensive assessment of model validity within the second term of the ELBO across the domain, we have to select the number of residuals N_c required and their spatial distribution. There are three possible strategies:

1. We preselect a set of constitutive-law residuals on a fixed grid, e.g., the nodes of the finite element grid used in Eq. 7. At each iteration, one could either incorporate all preselected residuals or employ a subsampling strategy, similar to the first term of ELBO, to balance computational efficiency with accuracy, or
2. We preselect a set of fixed, randomly distributed residuals in the domain and can again employ subsampling, or
3. We can employ an adaptive strategies, beginning with a uniform distribution and progressively refining residual selection in regions where $\left(\lambda_j^{(c)} \right)^{-1}$ is found to be large, thereby focusing computational effort on areas with higher model uncertainty.

We selected the first option without subsampling for this report, as it is the easiest to implement, and the problems considered are not limited by the number of $r^{(c)}$ considered due to their low dimensionality. We do not claim that this strategy is the best in accuracy or computational efficiency for other problems or even those considered in this report.

2.4 Approximate posterior

The approximate posterior q_{ξ} is critical for accuracy and efficiency, requiring a balance between expressiveness and computational simplicity. To motivate our choice, it is to note that solution field u , material field m , and stress field σ are strongly dependent as they must jointly ensure that the weighted residuals $r^{(e)}$ and constitutive law residuals $r^{(c)}$ in the virtual likelihoods are in the vicinity of zero (given that the select constitutive law is valid). The general structure of the posterior is thus

$$q_{\xi}(\mathbf{z}, \mathbf{x}, \boldsymbol{\chi}, \boldsymbol{\lambda}^{(c)}) = q_{\xi}(\mathbf{x}|\mathbf{z})q(\boldsymbol{\chi}|\mathbf{z})q(\mathbf{z})q(\boldsymbol{\lambda}^{(c)}) \quad (20)$$

To capture this connection, we use a latent variable z to represent the inner state of the system and connect its samples to the quantities mentioned above (see Figure 1):

$$q_{\xi}(z) = \mathcal{N}(z | \mu_z, \mathbf{S}_z) \quad (21)$$

Analogously to [25], we link the mean $\mu_{x;\xi_x}$ and $\mu_{\chi;\xi_\chi}$ to z via neural networks with parameters ξ

$$q_{\xi}(x|z) = \mathcal{N}(x | \mu_{x;\xi_x}(z), \mathbf{S}_x) \quad \text{and} \quad q_{\xi}(\chi|z) = \mathcal{N}(\chi | \mu_{\chi;\xi_\chi}(z), \mathbf{S}_\chi), \quad (22)$$

where the conditional covariance \mathbf{S}_x and \mathbf{S}_χ are assumed to be independent of z and of the form

$$\mathbf{S}_x = \mathbf{L}_x \mathbf{L}_x^T + \text{diag}(\sigma_x^2) \quad \text{and} \quad \mathbf{S}_\chi = \mathbf{L}_\chi \mathbf{L}_\chi^T + \text{diag}(\sigma_\chi^2), \quad (23)$$

where \mathbf{L}_x (or similarly \mathbf{L}_χ) is a matrix of dimension $d_x \times d_{\bar{x}}$ (or $d_\chi \times d_{\bar{\chi}}$) that captures the principal directions along which (conditional) variance is larger whereas σ_x^2 (or σ_χ^2) is a vector of dimension d_x (or d_χ) that captures the residual (conditional) variance along the x - (or χ -) dimensions. In contrast to a full covariance matrix, the form adopted for \mathbf{S}_x (or \mathbf{S}_χ) ensures linear scaling of the unknown parameters with d_x (or d_χ), which for most problems can be high.

Further, the approximate posterior for $\lambda^{(c)}$ is independent and given via

$$q_{\xi}(\lambda^{(c)}) = \prod_{j=1}^{d_{\lambda^{(c)}}} \text{Gamma}(\lambda_i^{(c)} | a_i, b_i), \quad (24)$$

to be able to update in closed form.

The resulting vector of parameters ξ that has to be optimized by maximizing the ELBO is given by

$$\xi = \{\mu_z, \mathbf{S}_z, \xi_x, \mathbf{L}_x, \sigma_x^2, \xi_\chi, \mathbf{L}_\chi, \sigma_\chi^2, \mathbf{a}, \mathbf{b}\}. \quad (25)$$

Remarks:

- There is an alternative formulation for u , where the representation does not rely on known basis functions but rather on learning the basis function using a neural network. The details, as well as the advantages, are discussed in Appendix A.

2.5 SVI

The ELBO $\mathcal{L}(\xi)$ is maximized using Stochastic Variational Inference (SVI), which relies on Monte Carlo estimates and Stochastic Gradient Ascent. The reparameterization trick is employed to generate samples from the approximate posterior q_{ξ} . Given the structure of q_{ξ} , this process begins by drawing z -samples from $q_{\xi}(z)$

$$z = \mu_z + \mathbf{S}_z \varepsilon_1 \quad \varepsilon_1 \sim \mathcal{N}(\mathbf{0}, \mathbf{I}_{d_z}), \quad (26)$$

which can be used as an input for the neural networks that approximate the means of x and χ to then generate random samples as

$$x = \mu_{x;\xi_x}(z) + \mathbf{L}_x \varepsilon_2 + \sigma_x \odot \varepsilon_3, \quad \varepsilon_2 \sim \mathcal{N}(\mathbf{0}, \mathbf{I}_{d_{\bar{x}}}) \quad \text{and} \quad \varepsilon_3 \sim \mathcal{N}(\mathbf{0}, \mathbf{I}_{d_x}) \quad \text{and} \quad (27)$$

$$\chi = \mu_{\chi;\xi_\chi}(z) + \mathbf{L}_\chi \varepsilon_4 + \sigma_\chi \odot \varepsilon_5, \quad \varepsilon_4 \sim \mathcal{N}(\mathbf{0}, \mathbf{I}_{d_{\bar{\chi}}}) \quad \text{and} \quad \varepsilon_5 \sim \mathcal{N}(\mathbf{0}, \mathbf{I}_{d_\chi}), \quad (28)$$

respectively. Lastly, sampling from $q_{\xi}(\lambda^{(c)})$ is straightforward, or when we follow the iterative updating scheme as in Appendix B, the expectancy can be evaluated in closed form by $\langle \lambda_i^{(c)} \rangle = \frac{a_i}{b_i}$.

We sample K tuples of $\{\chi, x, z\}$ to approximate the weighted residuals $r^{(e)}$ in Eq. 8, and J samples of $\lambda^{(c)}$ to then evaluate the constitutive law residual $r^{(c)}$ at J locations times K samples. The gradients are computed using PyTorch's automatic differentiation. Parameter updating is performed via ADAM with standard parameters and learning rate $\rho = 10^{-4}$. The pseudo-code is given in Algorithm 1.

Algorithm 1 SVI Training Algorithm

Select $\lambda^{(e)}$, τ , K , L ; Initialize $\xi \leftarrow \xi_0$, $t \leftarrow 0$
while \mathcal{L} not converged **do**
 Generate K weight functions $w^{(j_k)}$
 for $\ell = 1$ to L **do**
 Draw $z \leftarrow \mu_z + S_z \varepsilon_1$, $\varepsilon_1 \sim \mathcal{N}(\mathbf{0}, \mathbf{I}_{d_z})$
 $\mu_{n;\xi_x}, \mu_{n;\xi_\chi} \leftarrow NN_x(z_\ell), NN_\chi(z_\ell)$
 Draw $\mathbf{x}_\ell \leftarrow \mu_{x;\xi_x}(z_\ell) + \mathbf{L}_x \varepsilon_2 + \sigma_x \varepsilon_3$, $\varepsilon_2 \sim \mathcal{N}(\mathbf{0}, \mathbf{I}_{d_{\bar{x}}})$, $\varepsilon_3 \sim \mathcal{N}(\mathbf{0}, \mathbf{I}_{d_x})$
 Draw $\chi_\ell \leftarrow \mu_{\chi;\xi_\chi}(z_\ell) + \mathbf{L}_\chi \varepsilon_4 + \sigma_\chi \varepsilon_5$, $\varepsilon_4 \sim \mathcal{N}(\mathbf{0}, \mathbf{I}_{d_{\bar{\chi}}})$, $\varepsilon_5 \sim \mathcal{N}(\mathbf{0}, \mathbf{I}_{d_\chi})$
 end for
 Estimate $\mathcal{L}_\xi(\mathbf{x}_\ell, z_\ell, w^{(j_k)}, \chi_\ell)$
 Estimate $\nabla_\xi \mathcal{L}_\xi$
 Update $\xi_{t+1} \leftarrow \xi_t + \rho^{(t)} \odot \nabla_\xi \mathcal{L}_\xi$
 $t \leftarrow t + 1$
end while

2.6 Important quantities for the results

After convergence, we can sample $B = 1000$ tuples $\{z, \mathbf{x}, \chi, \lambda^{(c)}\}$ from the approximate posterior q_ξ and combine them with the basis functions (for $\{\mathbf{x}, \chi\}$) to receive material fields m and stress fields $\bar{\sigma}$, evaluate the neural network at grid locations to receive a solution field \mathbf{u} or order the parameters directly to their positions in the case of $\lambda^{(c)}$. In all cases, we are then able to estimate the posterior mean and variance via a location-point-wise Monte Carlo estimate of a quantity (\cdot)

$$\mathbb{E}[(\cdot)(\mathbf{s}) | \hat{\mathbf{u}}, \hat{\mathbf{R}}^{(c)}, \hat{\mathbf{R}}^{(e)}] \approx \frac{1}{B} \sum_{b=1}^B (\cdot)_b(\mathbf{s}) \quad \text{and} \quad (29)$$

$$\text{Var}[(\cdot)(\mathbf{s}) | \hat{\mathbf{u}}, \hat{\mathbf{R}}^{(c)}, \hat{\mathbf{R}}^{(e)}] \approx \frac{1}{B} \sum_{b=1}^B \left((\cdot)_b(\mathbf{s}) - (\hat{\cdot})(\mathbf{s}) \right)^2. \quad (30)$$

or estimate the credibility intervals (e.g. 2.5% and 97.5%) at each location as

$$Q_{0.025}((\cdot)(\mathbf{s})) = \text{quantile}((\cdot)_b(\mathbf{s}), 0.025) \quad \text{and} \quad (31)$$

$$Q_{0.975}((\cdot)(\mathbf{s})) = \text{quantile}((\cdot)_b(\mathbf{s}), 0.975). \quad (32)$$

3 Numerical Results

This section will consider a two-spacial-dimensional, synthetic problem, inverse problem to show the capabilities of the proposed framework. Our goals are as follows

- Show the capability of the framework to correctly identify regions where the assumed constitutive are valid/invalid and
- In parts of the domain where the constitutive equation is valid, the method should be able to identify the correct material parameters.

3.1 Problem setup and implementation details

The problem is modeled like an elastography problem, i.e., we aim to identify a Youngs Modulus field $m = E$ with inclusion in a constant background from noisy displacement observations $\hat{\mathbf{u}}$, where the problem is governed by the PDE in Eq. 1. The domain and boundary conditions are as shown in Figure 2. The synthetic data (ground truth) was generated with the finite element software Fenics on a triangular 128×128 grid. From this, displacement data $\hat{\mathbf{u}}$ was generated on a 32×32 grid, including the domain boundary, and contaminated with known Gaussian noise τ .

The discretization is as follows:

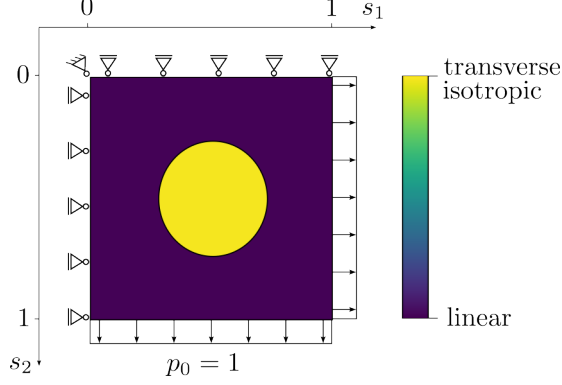


Figure 2: Problem setup.

- The Youngs modulus field $m = E$ as based on an element-wise constant triangular 32×32 grid, i.e., $\dim(\mathbf{x}) = 1922$,
- The stress field $\boldsymbol{\sigma}$ has three fields (σ_{11} , σ_{12} , and σ_{22}), each of which is modeled by an element-wise constant triangular 32×32 grid, i.e., $\dim(\boldsymbol{\chi}) = 5766$,
- The weight functions \mathbf{w} are two linear triangular elements on a 32×32 grid, i.e., $\dim(\mathbf{w}) = 2048$.
- The displacement field is modeled by a 7-layer neural network with 40 neurons and a tanh activation function each, which takes the position vector \mathbf{s} as an input. The last layer has a sigmoid activation function and 50 outputs, multiplied with \mathbf{z} to obtain the value \mathbf{u} at a given location.

All priors are modeled independently and are selected as follows:

- We employ a standard normal prior on \mathbf{z} : $p(\mathbf{z}) = \prod_{i=1}^{\dim(\mathbf{z})} \mathcal{N}(z_i|0, 1)$
- We employ an informative prior on $\boldsymbol{\chi}$, as we have no information about its value a-prior: $p(\boldsymbol{\chi}) = \prod_{i=1}^{\dim(\boldsymbol{\chi})} \mathcal{N}(\chi_i|0, 10^{16})$
- For \mathbf{x} , we denote with $\mathbf{J}_x = \mathbf{B} \mathbf{x}$ the vector of jumps between neighboring points of dimension d_{jumps} . We imposed a hierarchical prior on \mathbf{J}_x that consists of:

$$p(\mathbf{x}|\boldsymbol{\theta}) = \mathcal{N}(\mathbf{J}_x | \mathbf{0}, \text{diag}(\boldsymbol{\theta}^{-1}))$$

$$p(\boldsymbol{\theta}) = \prod_{j=1}^{d_{jumps}} \text{Gamma}(\theta_j | a_0 = 10^{-8}, b_0 = 10^{-8}). \quad (33)$$

The precision hyper-parameters $\boldsymbol{\theta}$ promote sparsity in the number of jumps, i.e., piece-wise constant solutions [26].

- For $\boldsymbol{\lambda}^{(c)}$, we select a similar Gamma prior, so we can update the posterior later in closed form as described in Appendix B: $p(\boldsymbol{\lambda}^{(c)}) = \prod_{j=1}^{d_{\lambda^{(c)}}} \text{Gamma}(\lambda_j^{(c)} | a_0 = 10^{-8}, b_0 = 10^{-8})$.

The approximate posterior q_{ξ} will be constructed as noted in section 2.4. We employ the following architectures:

- The mean $\boldsymbol{\mu}_{\mathbf{x}; \boldsymbol{\xi}_x}$ takes the 50 \mathbf{z} values as input for a 3-hidden-layer neural network with 2000 neurons and SiLU activation function in each layer. The reduced dimension for the covariance matrix is $\times d_{\tilde{\mathbf{x}}} = 10$.
- The mean $\boldsymbol{\mu}_{\boldsymbol{\chi}; \boldsymbol{\xi}_x}$ takes the 50 \mathbf{z} values as input for a 3-hidden-layer neural network with $\{3000, 4000, 6000\}$ neurons and SiLU activation function in each layer. The reduced dimension for the covariance matrix is $\times d_{\tilde{\boldsymbol{\chi}}} = 10$.

For weight functions \mathbf{w} , we subsample $K = 200$ out of $N = 24,576$ in each iteration, constructed similarly as in [25]. Further, we samples $L = 10$ tuples of $\{\mathbf{z}, \mathbf{x}, \boldsymbol{\chi}\}$ per iterations. We select $\lambda^{(e)} = 10^{10}$. The program is implemented in PyTorch and trained on a Nvidia RTX 4090 GPU.

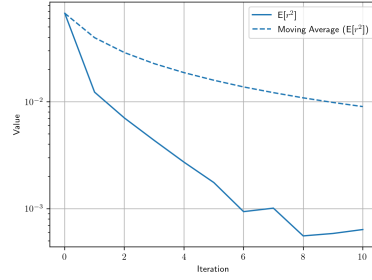


Figure 3: Expected weighted squared residual $r^{(c)}$ over the iterations (1 unit = 10, 000 iterations)

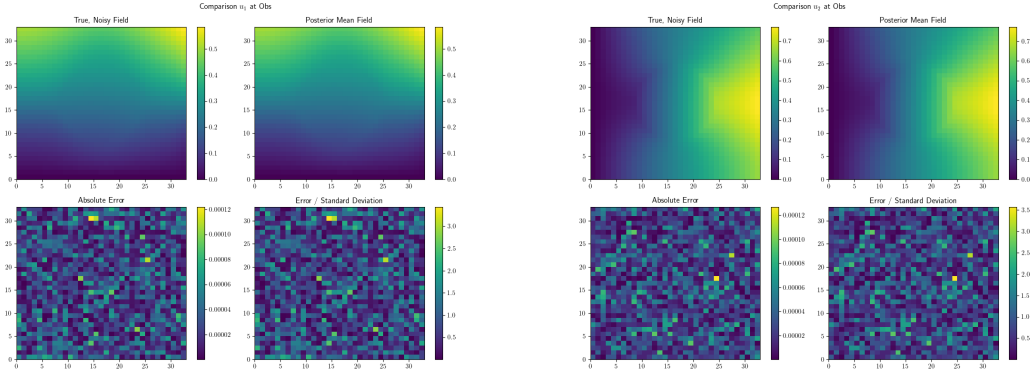


Figure 4: Displacement fields u_1 (left) and u_2 (right). On both subfigures: The observations \hat{u} are in the top left, the inferred posterior mean of the displacement fields μ_{u_i} are in the top right, the absolute error of these two are in the bottom left, and the absolute errors normed by the observation noise τ^{-1} are the bottom right subplot.

3.2 Experiment I)

In this experiment, the ground truth material field consists of a background with linear elastic material behavior governed by

$$\boldsymbol{\sigma} = \lambda \varepsilon_{kk} \delta_{ij} + 2\mu \varepsilon_{ij}, \quad (34)$$

where $\varepsilon_{ij} = 0.5 (\nabla \mathbf{u} + (\nabla \mathbf{u})^T)$ and λ and μ are first and second Lamé parameters, which relate to the Young's Modulus field as $\lambda = \nu E / ((1 - 2\nu)(1 + \nu))$ and $\mu = E / (2(1 + \nu))$, with constant $\nu = 0.3$ and $E = 1.0$. Within this background is a circular inclusion with a radius $r = 0.2$, which is governed by a transversely isotropic material behavior (formula in Appendix C), where the vertical stiffness is $E_{\text{vert}} = 3.0$ and the horizontal stiffness is $E_{\text{hor}} = 1.0$. The inverse problem model, however, assumes a linear elastic material behavior over the whole domain.

The convergence of our method can be observed in Figure 3, where the expected squared weighted residual $r^{(c)}$ drops by two orders of magnitude during the simulation. Further, the inferred displacement fields \mathbf{u} are depicted in Figure 4, where the posterior fields coincide with the observations.

From the stress fields $\boldsymbol{\sigma}$ in Figure 5, we can see that the stresses in the inclusion in the vertical direction (σ_{11}) are higher than in the horizontal direction (σ_{22}), due to the transverse-isotropic material behavior there. In contrast, the algorithm predicts a constant Young's Modulus E over the whole domain, as in Figure 6, which can not capture material behavior dictated by the stresses $\boldsymbol{\sigma}$ inferred from the conservation law. Thus, we turn to the last plot, which shows us the precision parameter $\lambda^{(c)}$ located at the finite element grid node points in Figure 6. This parameter determines how tightly the predicted stresses by the conservation law $\boldsymbol{\sigma}$ coincide with the stresses predicted by the constitutive equation $\tilde{\boldsymbol{\sigma}}$. The plot shows that the algorithm gives the expected result, i.e., the

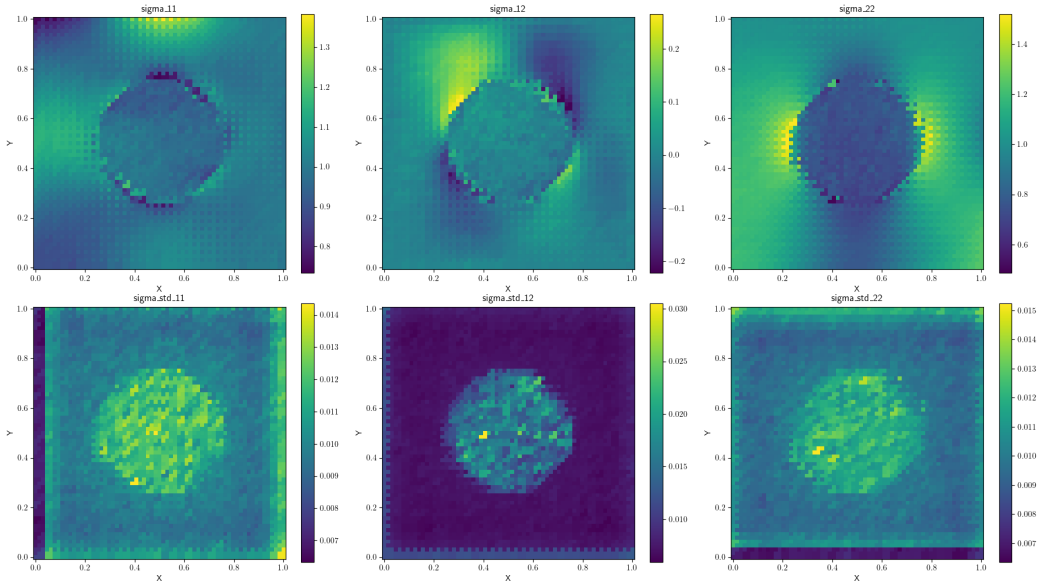


Figure 5: First line shows the stress means μ_{σ} and second line shows the 95% credibility intervals. In the columns (f.l.t.r.) are shown the components σ_{11} , σ_{12} and σ_{22} .

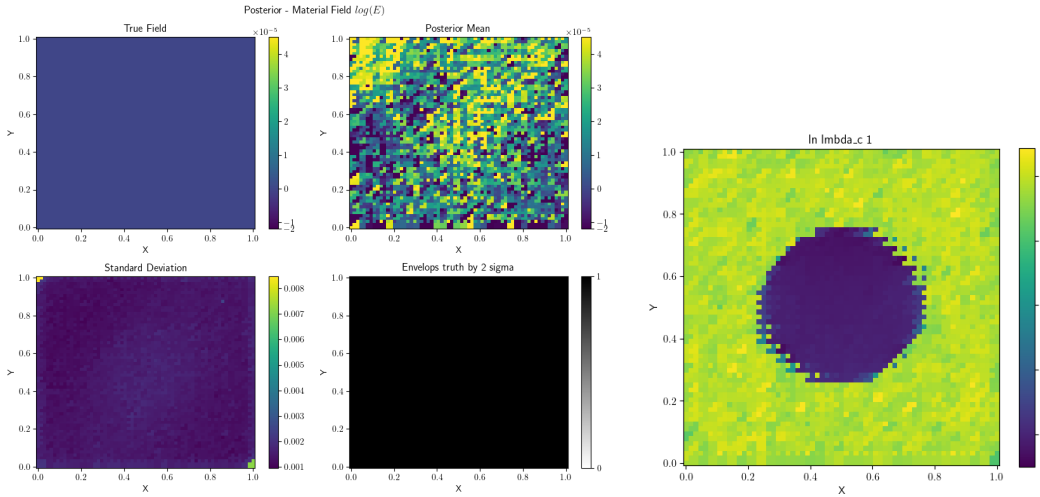


Figure 6: Shows Logarithmic Young's modulus field $\ln E$ on the left and the precision $\lambda^{(c)}$ on the right. In the left subplot, the top left plot shows the true field (but transverse isotropic cannot be depicted), the top right shows the approximate posterior mean, the bottom left shows the 95% credibility intervals, and the bottom right shows where approximation envelopes the ground truth.

material law is not valid for the (transverse-isotropic) inclusion. At the same time, it is valid for the linear-elastic background material.

4 Discussion and Outlook

In this study, we demonstrated the effectiveness of our framework in identifying regions where the prescribed material law did not hold using the precision parameter. In regions where the material law was valid, the predicted material parameters were correctly inferred, while in invalid regions, the applied prior flattened the field, preventing inaccurate predictions. Additionally, the inferred stress fields adhered to the conservation law, further validating our approach.

Our method enabled fast inference by leveraging the weighted residual scheme proposed by Scholz et al., demonstrating its computational efficiency. However, several avenues remain for future work.

To further validate and extend our approach, we plan to:

- Conduct experiments on higher-dimensional grids (e.g., 64×64 resolution).
- Test the framework using real or phantom data to assess its practical applicability.
- Investigate scenarios with multiple inclusions, including one with a valid and one with an invalid material law. Initial tests showed that both inclusions were flagged as invalid, highlighting a need for refinement.
- Implement latent-based fields to downscale large neural networks and improve computational efficiency.

These future investigations will enhance the framework's robustness and broaden its applicability in inverse modeling problems.

References

- [1] J. Ophir, I. Cespedes, H. Ponnekanti, Y. Yazdi, X. Li, Elastography: a quantitative method for imaging the elasticity of biological tissues, *Ultrasonic imaging* 13 (2) (1991) 111–134.
- [2] M. M. Doyley, Model-based elastography: a survey of approaches to the inverse elasticity problem, *Physics in Medicine & Biology* 57 (3) (2012) R35.
- [3] R. Muthupillai, D. Lomas, P. Rossman, J. F. Greenleaf, A. Manduca, R. L. Ehman, Magnetic resonance elastography by direct visualization of propagating acoustic strain waves, *science* 269 (5232) (1995) 1854–1857.
- [4] A. S. Khalil, R. C. Chan, A. H. Chau, B. E. Bouma, M. R. K. Mofrad, Tissue elasticity estimation with optical coherence elastography: toward mechanical characterization of in vivo soft tissue, *Annals of biomedical engineering* 33 (2005) 1631–1639.
- [5] M. Raissi, P. Perdikaris, G. E. Karniadakis, Physics-informed neural networks: A deep learning framework for solving forward and inverse problems involving nonlinear partial differential equations, *Journal of Computational physics* 378 (2019) 686–707.
- [6] C. R. Vogel, *Computational methods for inverse problems*, SIAM, 2002.
- [7] P. J. Green, K. Łatuszyński, M. Pereyra, C. P. Robert, Bayesian computation: a summary of the current state, and samples backwards and forwards, *Statistics and Computing* 25 (2015) 835–862.
- [8] D. M. Blei, A. Kucukelbir, J. D. McAuliffe, Variational inference: A review for statisticians, *Journal of the American statistical Association* 112 (518) (2017) 859–877.
- [9] J. Brynjarsdóttir, A. O'Hagan, Learning about physical parameters: The importance of model discrepancy, *Inverse problems* 30 (11) (2014) 114007.
- [10] J. Kaipio, E. Somersalo, *Statistical and computational inverse problems*, Vol. 160, Springer Science & Business Media, 2006.
- [11] G. A. Holzapfel, Similarities between soft biological tissues and rubberlike materials, in: *Constitutive models for rubber IV*, Routledge, 2017, pp. 607–617.

- [12] M. C. Kennedy, A. O’Hagan, Bayesian calibration of computer models, *Journal of the Royal Statistical Society: Series B (Statistical Methodology)* 63 (3) (2001) 425–464.
- [13] L. M. Berliner, K. Jezek, N. Cressie, Y. Kim, C. Q. Lam, C. J. Van Der Veen, Modeling dynamic controls on ice streams: a bayesian statistical approach, *Journal of Glaciology* 54 (187) (2008) 705–714.
- [14] D. Andrés Arcones, M. Weiser, P.-S. Koutsourelakis, J. F. Unger, Model bias identification for bayesian calibration of stochastic digital twins of bridges, *Applied Stochastic Models in Business and Industry* (2024).
- [15] P. Pernot, F. Cailliez, A critical review of statistical calibration/prediction models handling data inconsistency and model inadequacy, *AIChE Journal* 63 (10) (2017) 4642–4665.
- [16] P. Pernot, The parameter uncertainty inflation fallacy, *The Journal of Chemical Physics* 147 (10) (2017).
- [17] K. Sargsyan, H. N. Najm, R. Ghanem, On the statistical calibration of physical models, *International Journal of Chemical Kinetics* 47 (4) (2015) 246–276.
- [18] K. Sargsyan, X. Huan, H. N. Najm, Embedded model error representation for bayesian model calibration, *International Journal for Uncertainty Quantification* 9 (4) (2019).
- [19] R. E. Kass, A. E. Raftery, Bayes factors, *Journal of the american statistical association* 90 (430) (1995) 773–795.
- [20] C. Hoerig, J. Ghaboussi, Y. Wang, M. F. Insana, Machine learning in model-free mechanical property imaging: Novel integration of physics with the constrained optimization process, *Frontiers in Physics* 9 (2021) 600718.
- [21] W. Newman, J. Ghaboussi, M. Insana, Improving image quality in a new method of data-driven elastography, in: *Medical Imaging 2024: Ultrasonic Imaging and Tomography*, Vol. 12932, SPIE, 2024, pp. 51–56.
- [22] P.-S. Koutsourelakis, A novel bayesian strategy for the identification of spatially varying material properties and model validation: an application to static elastography, *International Journal for Numerical Methods in Engineering* 91 (3) (2012) 249–268.
- [23] L. Bruder, P.-S. Koutsourelakis, Beyond black-boxes in bayesian inverse problems and model validation: applications in solid mechanics of elastography, *International Journal for Uncertainty Quantification* 8 (5) (2018).
- [24] S. Kaltenbach, P.-S. Koutsourelakis, Incorporating physical constraints in a deep probabilistic machine learning framework for coarse-graining dynamical systems, *Journal of Computational Physics* 419 (2020) 109673.
- [25] V. C. Scholz, Y. Zang, P.-S. Koutsourelakis, Weak neural variational inference for solving bayesian inverse problems without forward models: applications in elastography, *Computer Methods in Applied Mechanics and Engineering* 433 (2025) 117493.
- [26] J. M. Bardsley, J. Kaipio, Gaussian markov random field priors for inverse problems., *Inverse Problems & Imaging* 7 (2) (2013).

A Alternative Formulation of the Proposed Method

This alternative formulation focuses on how the fields are constructed from random variables, with particular emphasis on how the latent variable \mathbf{z} generates the displacement field \mathbf{u} . Instead of relying on predefined basis functions $\boldsymbol{\eta}_i^{\mathbf{u}}(\mathbf{s})$, we propose learning a set of basis functions via a neural network with parameters $\xi_{\mathbf{u}}$:

$$\mathbf{u} = \sum_{i=1}^{d_{\mathbf{z}}} \mathbf{z}_i \text{NN}_{\xi_{\mathbf{u}}}(\mathbf{s}). \quad (35)$$

Here, the neural network $\text{NN}_{\xi_{\mathbf{u}}}(\mathbf{s})$ takes the position \mathbf{s} as input and, through a dot product with the latent variable \mathbf{z} , generates the function value $\mathbf{u}(\mathbf{s})$. A key advantage of this approach is its computational efficiency, as it enables capturing the statistical variations in the displacement field \mathbf{u} with a lower-dimensional representation of \mathbf{z} compared to the standard formulation. This efficiency arises from the enhanced expressiveness of the learned basis functions relative to traditional finite element shape functions.

This reformulation also alters the role of the random variable z within the framework. It now serves as a latent representation of the system’s internal state, influencing the tuple $\{m, \mathbf{u}, \sigma\}$. Unlike the approach presented in Section 2, where z primarily contributes to field construction, the task of forming \mathbf{u} is now shifted toward the neural network representing the basis functions. Additionally, as z serves as an input to the neural networks computing the means of σ and x , its lower dimensionality results in a reduced number of required parameters in these networks.

While other fields, such as m and σ , can also be parameterized using neural networks to further reduce parameter count, this introduces additional challenges. In particular, handling sharp inclusion boundaries necessitates an appropriate prior, as conventional finite element-based penalties for abrupt jumps between neighboring elements are no longer applicable. These challenges do not arise for the displacement field \mathbf{u} , which is inherently smooth.

A limitation of this formulation is that domain integration is no longer feasible in closed form, as was possible with predefined basis functions. Consequently, Monte Carlo integration must be employed. To assess its impact, we conducted a study on how the number of Monte Carlo integration points influences noise in residual calculations (for 10 different weight functions and 10 random realizations of \mathbf{x}, z, χ), summarized in Table 1. In some first studies, we thus use 500 MC integration points to approximate the integrals, as it balances efficiency and accuracy.

| # MC Points | $\ \Delta r^{(c)}\ _2^2$ |
|-------------|--------------------------|
| 10,000 | 0.0 (ground truth) |
| 5,000 | 0.87 |
| 1,000 | 2.81 |
| 500 | 2.89 |
| 100 | 10.05 |
| 50 | 11.38 |
| 10 | 30.71 |

Table 1: Effect of Monte Carlo integration points on residual noise.

B Closed form updating of constitutive law precision

The ill-posed nature of the problem arises from the fact that there are no direct observations of the stresses σ , only noisy displacement fields \mathbf{u} . This leads to an underdetermined system, requiring regularization to recover meaningful solutions. To address this, we employ an Automatic Relevance Determination (ARD) prior on the precision parameters $\lambda^{(c)}$. We aim to use the prior to preferring solutions in which the given material law is assumed to be correct unless strong evidence speaks against it, thus encouraging large values for $\lambda^{(c)}$.

Therefore, note that the Gaussian virtual constitutive likelihood $p(\hat{\mathbf{R}}^{(c)} | z, \mathbf{x}, \chi, \lambda^{(c)})$ and the Gamma prior on $\lambda^{(c)}$ are conjugate, we can select a Gamma posterior as a natural choice. This enables us to update the approximate posterior $q_{\xi}(\lambda^{(c)})$ in closed form as

$$a_{\lambda_i^{(c)}} = a_0 + \frac{1}{2}, \quad \text{and} \quad b_{\lambda_i^{(c)}} = b_0 + \frac{1}{2} \mathbb{E}_{q_{\xi}} \left[\left(r_i^{(c)} \right)^2 \right]. \quad (36)$$

We then iteratively update the approximate posterior using the following scheme:

1. Updating the approximate posterior $q_{\xi}(\lambda^{(c)})$ according to (36) given samples of $\{z, \mathbf{x}, \chi\}$, and
2. Updating the approximate posterior $q(z, \mathbf{x}, \chi)$ according to the SVI scheme introduced in section 2, where we can calculate $\langle \lambda_i^{(c)} \rangle = \frac{a_{\lambda_i^{(c)}}}{b_{\lambda_i^{(c)}}$ in closed form.

C Transversaly isotropic material law

A transversely isotropic material is one with physical properties that are symmetric about an axis \mathbf{a} , while the properties in said direction may differ. In our case, we define the axis as $\mathbf{a} = [1 \ 0]$,

in which the Youngs Modulus is $E_a = 3.0$ and the shear modulus $G_a = 1.154$, compared to the direction perpendicular to it, where the Youngs Modulus is chosen to be $E = 1.0$. We assume the same Poissons ratio of $\nu = \nu_a = 0.3$ in all directions. From this we can calculate the following intermediate quantities:

$$n = E_a/E \quad (37)$$

$$m = 1 - \nu - 2n\nu^2 \quad (38)$$

$$\lambda = E(\nu + n\nu^2)/(m(1 + \nu)) \quad (39)$$

$$\mu = E/(2(1 + \nu)) \quad (40)$$

$$\alpha = \mu - G_a \quad (41)$$

$$\beta = E\nu^2(1 - n)/(4m(1 + \nu)) \quad (42)$$

$$\gamma = E_a(1 - \nu)/(8m) - (\lambda + 2\mu)/8 + \alpha/2 - \beta. \quad (43)$$

We define the deformation gradient $\mathbf{F} = \mathbf{I} + \nabla \mathbf{u}$ and use it to evaluate the left and right Cauchy-Green tensors as $\mathbf{B} = \mathbf{F}\mathbf{F}^T$ and $\mathbf{C} = \mathbf{F}^T\mathbf{F}$. Further, the Jacobian can be calculated as $J = \det \mathbf{F}$, and the invariants required are

$$I_1 = \text{tr} \mathbf{C} \quad (44)$$

$$I_4 = \mathbf{a} \cdot \mathbf{C} \mathbf{a} \quad (45)$$

$$\mathbf{A} = \mathbf{a} \otimes \mathbf{a}. \quad (46)$$

Then, the stress tensor $\boldsymbol{\sigma}_{\text{trans}}$ can be calculated by

$$\begin{aligned} \boldsymbol{\sigma}_{\text{trans}} = & \frac{1}{J}(2\beta(I_4 - 1)\mathbf{B} \\ & + 2(\alpha + \beta(I_1 - 2) + 2\gamma(I_4 - 1))\mathbf{A} \\ & - \alpha((\mathbf{B}\mathbf{a}) \otimes \mathbf{a} + \mathbf{a} \otimes (\mathbf{B}\mathbf{a})) \\ & \mu/J(\mathbf{B} - \mathbf{I}) + \lambda(J - 1)\mathbf{I} \end{aligned}$$